Controls on the Development and Circulation of Terminal versus Transient Congestus Clouds and Implications for Midlevel Aerosol Transport

GABRIELLE R. LEUNG[a] AND SUSAN C. VAN DEN HEEVER[a]

[a] *Department of Atmospheric Science, Colorado State University, Fort Collins, Colorado*

ABSTRACT: Cumulus congestus is the middle mode of tropical convection, with cloud tops around or exceeding the 0°C level (~5 km AGL). While some congestus are terminal, meaning capped by the 0°C stable layer, others are transient and may develop into deep convection. Although this distinction impacts convective transport of water vapor and aerosols into the midtroposphere and the congestus to deep convection transition, there is still much to be understood about the processes causing congestus to overshoot the 0°C level and continue growing. We simulate a field of tropical congestus using high-resolution idealized model simulations, identify and track the updrafts, and composite congestus properties. Terminal and transient congestus updrafts are characterized by a similar overturning circulation between the updraft and subsiding shell. However, transient congestus have stronger updrafts, and the downward branch of their corresponding circulations are constrained by the 0°C level. The balance between buoyancy and perturbation pressure gradient accelerations predominantly determines the shape of the vertical velocity profile, though vertical advection through bulk and subplume fluctuations are also shown to be important near and above the 0°C level. Our findings support previous results suggesting buoyancy as a control on congestus height. We find that congestus developing in more humid midlevel environments are more likely to be transient. Finally, we explore how congestus updrafts influence their near moisture and aerosol environments: terminal congestus return more aerosol to the atmosphere through evaporation along their edges, while transient congestus create stronger midlevel detrainment layers of aerosol and water vapor due to the trapping of the regenerated aerosol above the 0°C level.

KEYWORDS: Tropics; Cumulus clouds; Aerosols; Mass fluxes/transport; Momentum

1. Introduction

The three modes of tropical convection—shallow cumulus, cumulus congestus, and deep convection—are capped by layers of increased static stability at the trade wind inversion (~2 km AGL), the 0°C stable layer (~5 km AGL), and the tropopause (~15–16 km AGL), respectively (Johnson et al. 1999; Masunaga et al. 2005; Posselt et al. 2008). The congestus mode is relatively understudied compared to shallow cumulus and deep convection, but is still of interest due to its role as an intermediary in the transition from shallow to deep convection (Mapes et al. 2006; Waite and Khouider 2010), its capacity to flux mass and energy into the midlevels (Kuang and Bretherton 2006; Takayabu et al. 2010), and its significant contribution to tropical precipitation (Lau and Wu 2003; Jensen and Del Genio 2006; van den Heever et al. 2011). Furthermore, because their updrafts are somewhat weaker than deep convective clouds, congestus are also more susceptible to aerosol forcing than faster and deeper updrafts (Li et al. 2013; Sheffield et al. 2015). Understanding the factors that govern congestus development and their potential transition into deep convection is therefore important for improving scientific understanding and model representation of tropical convection.

Within the congestus mode it is important to distinguish between what are referred to as terminal and transient congestus (Luo et al. 2009) in order to enhance our understanding of both convective detrainment and the shallow to deep convection transition. In Johnson et al. (1999), congestus are identified in relation to the 0°C stable layer, but they also found considerable numbers of congestus overshooting this level. Luo et al. (2009) defined terminal congestus as those which have ceased to develop vertically past this 0°C stable layer (~4–6 km AGL). Terminal congestus typically detrain around that stable layer, which is formed from the melting of hydrometeors from dissipating anvil clouds and other mixed-phase clouds (Johnson et al. 1999) and sustained by clear-air subsidence and radiative cooling (Posselt et al. 2008). On the other hand, transient congestus penetrate this stable layer and continue developing aloft. These transient congestus may later become deep convective clouds if the additional latent heat released in the mixed-phase regions above the 0°C level sufficiently increases the updraft buoyancy (Johnson et al. 1999; Li et al. 2013; Sheffield et al. 2015; Mecikalski et al. 2016). The development of congestus above the 0°C level, and subsequent latent heat release in mixed-phase regions, has implications for the flux of energy and moisture into the midlevels and beyond, since ice processes are crucial to the mechanisms by which tropical convection drives large-scale circulations such as the Hadley cell (Riehl and Malkus 1958; Zipser 2003; Fierro et al. 2009; McGee and van den Heever 2014). The proportion of congestus clouds that are transient may also impact the vertical transport of boundary layer air, water vapor, energy, and aerosols, into the mid- and upper levels of the troposphere (Dawe and Austin 2011; Reid et al. 2019), from where they may subsequently influence other cloud processes including new cloud formation.

Traditionally, the differences in development between terminal and transient congestus have been attributed to buoyancy, which has been used in remote sensing studies to identify which congestus are likely to continue developing (Luo et al. 2009). It is thought that terminal congestus either have less low-level environmental convective available potential energy (CAPE) to begin with; are limited by the entrainment of dry air above the boundary layer, which leads to evaporation of droplets and a subsequent reduction in buoyancy; or are unable to regain positive buoyancy upon encountering the 0°C stable layer (Redelsperger et al. 2002). There is some observational and modeling evidence to support the dominant role of dry air entrainment in governing congestus buoyancy and overall height, showing that the cloud-top height (CTH) distribution is more strongly correlated with midlevel humidity than low-level CAPE or the magnitude of midlevel stability (Redelsperger et al. 2002; Takemi et al. 2004; Jensen and Del Genio 2006). However, the prior focus on correlations between environmental parameters and the population CTH distribution have not included establishing the mechanisms by which the environment influences the development of individual congestus clouds or ensembles of congestus. Momentum budgets have been analyzed for thermals and deep convective clouds. In general, these studies agree that the primary forces acting on thermals and on steady-state cloud ensembles are buoyancy and perturbation pressure gradient forces (PPGF), with lesser contributions from momentum entrainment (de Roode et al. 2012; Sherwood et al. 2013; Romps and Charn 2015; Peters 2016; Morrison and Peters 2018; Tian et al. 2019), although the relative magnitudes of each force depend on whether the full cloud volume or only the updraft volume is being considered (Wang and Zhang 2014; Savre 2021). While such momentum budgets have been analyzed for thermals and deep convection, similar momentum budget analysis has not been conducted specifically for congestus clouds. A more detailed analysis of congestus updraft momentum budgets would therefore be valuable, especially for potential applications to cumulus parameterizations. The physical mechanisms that govern whether a congestus cloud becomes transient or remains terminal—in particular, whether this can be determined by buoyancy alone—are still not yet well understood. Determining controls on congestus cloud-top height will help to improve model representations of convective development processes, cloud-top height distributions, as well as the overall energy and moisture budgets, and will allow us to assess how these may change in a warming climate. A better understanding of congestus acceleration budgets would also aid in understanding the physical processes behind aerosol impacts on congestus and how these are represented in models (Sheffield et al. 2015; Marinescu et al. 2021), though specific work on aerosol impacts on congestus is left for a future study.

In this work, we attempt to better characterize the dynamical and microphysical processes governing congestus development. Particular focus is given to identifying those factors which differentiate transient and terminal congestus, and how those differences impact the detrainment of water vapor and aerosols from congestus into the midlevels. Specifically, this study aims to answer two questions: 1) What physical mechanisms allow transient congestus to overshoot the 0°C level and continue developing while terminal congestus are capped? And 2) how does congestus cloud-top height relative to the 0°C level impact the detrainment of water vapor and aerosols? An idealized, high-resolution large-eddy simulation (LES) of a tropical congestus field provides a robust sample of congestus updrafts to identify, composite, and analyze. Differences between transient and terminal composites are explored in terms of updraft and near-environment structure, as well as the physical processes governing those distributions. Finally, the differences in the circulations of terminal and transient congestus are explored in terms of their implications for convective transport of aerosol particles, specifically in terms of their impact on midlevel detrainment of aerosol and water vapor.

2. Model description and analysis approach

a. Model description

We perform the simulations for this study with the Regional Atmospheric Modeling System (RAMS) (Cotton et al. 2003; Saleeby and van den Heever 2013), a nonhydrostatic cloud-resolving model with advanced microphysics and aerosol schemes. RAMS uses a two-moment, bin-emulating bulk microphysics scheme. Cloud water, rainwater, and five ice hydrometeor species (pristine ice, snow, aggregates, graupel, and hail) were enabled to capture both the warm and mixed-phase processes found in congestus clouds. Cloud droplets are activated from available cloud condensation nuclei (CCN) when sufficient water supersaturation is achieved. In the mixed phase, cloud water can be transferred to ice species by contact nucleation, riming, the Wegner–Bergeron–Findeisen process, and homogeneous freezing (Saleeby and Cotton 2008; Saleeby and van den Heever 2013). Heterogeneous nucleation via deposition nucleation, condensation freezing, and immersion freezing are parameterized for temperatures below 0°C based on DeMott et al. (2010).

RAMS aerosol mass budget capabilities were also enabled to further track the proportion of aerosol in four categories: 1) unprocessed aerosol, 2) in-hydrometeor aerosol, 3) regenerated aerosol, and 4) surface-accumulated aerosol (Saleeby and van den Heever 2013). Aerosol particles are removed from the domain upon the activation of cloud droplets, which transfers the aerosol mass to an in-cloud category and then to other in-hydrometeor categories as cloud mass is transferred between liquid and ice hydrometeors. Hydrometeor evaporation under subsaturated conditions transfers the in-hydrometeor aerosol mass to a regenerated aerosol category. Those aerosols that are not activated remain in the unprocessed aerosol category. The amount of aerosol accumulated onto the surface via wet deposition is also tracked. Aerosol particles can be advected around the domain and a negligible proportion of the initial aerosol mass is lost to diffusion and dry deposition. Additional details about the representation of aerosol processes are available in Saleeby and van den Heever (2013).

b. Model configuration and initialization

The idealized simulations were run over a fully oceanic domain with a fixed sea surface temperature and doubly periodic lateral boundaries. The domain was 100 km × 100 km in the horizontal with a grid spacing of 100 m. The vertical grid consisted of 120 levels spanning ~15 km, with grid spacing stretching from 50 to 200 m. There are 18 model levels between the surface and 1 km, and 63 model levels between the surface and the 0°C level (~5.1 km). The simulation was run for 48 h from 0000 UTC (0800 local time), with a time step of 0.75 s and output files produced every 5 min. This high spatiotemporal resolution allows the model to resolve large turbulent eddies and capture the detailed horizontal and vertical structure of congestus updrafts, subsiding shells, and detrainment layers (Peters et al. 2019; Savre 2021). Surface fluxes of heat and moisture are prognosed using the LEAF-3 submodel (Walko et al. 2000).

Initial conditions were horizontally homogeneous and based on a dropsonde from the Cloud, Aerosol, and Monsoon Processes Philippines Experiment (CAMP²Ex) (Reid et al. 2022, manuscript submitted to *Bull. Amer. Meteor. Soc.*). This dropsonde was selected because it sampled the tropical maritime environment near several congestus clouds, and because it allowed a congestus field to develop for several hours before transitioning toward deeper convective modes. The dropsonde was taken at approximately 0300 UTC, close to the initialization time of the model. The dropsonde profile was vertically smoothed by taking the mean value every 150 m to reduce sudden discontinuities in the data while maintaining the observed stable layers. To represent atmospheric information above the dropsonde launch altitude, ERA5 data from the same time period were averaged over a 1° × 1° box containing the congestus field (8°–9°N, 119°–120°E). A weighted average of the dropsonde and ERA5 profiles was taken between 5 and 6 km AGL, such that the resulting profile tapered off linearly between the dropsonde profile at 5 km AGL to the ERA5 profile at 6 km AGL. The resulting smoothed sounding, representing conditions favorable to the development of congestus over the ocean in the Maritime Continent (Reid et al. 2022, manuscript submitted to *Bull. Amer. Meteor. Soc.*), is shown in Fig. 1. Additional observational context of congestus clouds from CAMP²Ex that are similar to the clouds simulated in this paper can be found in Reid et al. (2022, manuscript submitted to *Bull. Amer. Meteor. Soc.*). It should be noted that there is vertical wind shear between 550 and 450 hPa, which has been found to promote the formation of congestus over deep convection (Tian et al. 2021). Random thermal perturbations with a maximum amplitude of 0.1 K were introduced within 500 m AGL of the lowest model level above the surface to initiate convection.

Sulfate aerosol particles were initialized horizontally homogeneously and decrease exponentially with height starting from a maximum surface number concentration of 500 mg^{-1}. Ice nuclei were initialized with the same distribution but starting from a maximum number concentration of 0.01 mg^{-1}. The size distribution of sulfate aerosol particles was represented as a lognormal with a median radius of 0.09 microns and a geometric standard
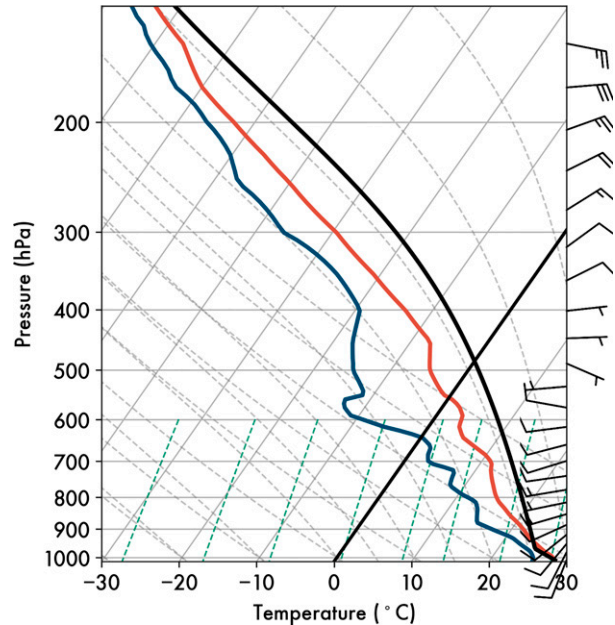

FIG. 1. Skew *T*–log*p* diagram showing the sounding and wind profile (m s^{-1}) used to initialize the numerical experiments. The black diagonal line indicates the freezing level. The solid black curve is a parcel trajectory from the surface.

deviation of 1.8, both of which are representative of the aerosol distributions measured in CAMP²Ex (Reid et al. 2022, manuscript submitted to *Bull. Amer. Meteor. Soc.*). Aerosol–radiation and microphysical–radiation interactions were included in the simulation. After initialization, the model is allowed to evolve freely with no additional large-scale forcing applied. The diurnal cycle of radiation is represented using the Harrington two-stream radiation scheme, updated every 5 min (Harrington 1997). The longitudinal variation of shortwave radiation is also represented (Saleeby and van den Heever 2013). Further details about the model setup are summarized in Table 1.

c. Congestus identification

Convection develops in the simulation ~5 h after initialization. Congestus clouds develop 2.5 h after the onset of shallow cumulus (shown by the contours in Fig. 2a that reach above 4 km AGL and a coincident increase in updraft velocities in Fig. 2b). The first 7.5 h of the simulation before congestus clouds develop are treated as model spinup time and excluded from the analysis. Figure 3 shows a sample of the simulated cloud field at one time step. Although deep convection is limited in this simulation, the congestus clouds appear alongside shallower cumulus and must be separated from these other types of clouds in the simulation to facilitate the analysis. To investigate the microphysical and dynamical characteristics of the updraft core of active congestus, we only perform the analysis on cells which are cloudy (defined as having cloud liquid + ice condensate with mixing ratios greater than 0.01 g kg^{-1}) and have updrafts (defined as having vertical velocity greater than 1 m s^{-1}).

TABLE 1. RAMS model options used in simulation.

Model aspect	Setting
Grid	Arakawa C grid
	1000×1000 points, $\Delta x = \Delta y = 100$ m
	120 vertical levels, $\Delta z = 50$–200 m
Time integration	48-h simulation duration, $\Delta t = 0.75$ s
Initialization	Horizontally homogeneous thermodynamic and wind profile, averaged from ERA5 and CAMP^{2}Ex dropsonde
	Random potential temperature perturbations within the lowest 500 m AGL of the domain, with a maximum perturbation of 0.1 K
Surface scheme	All-ocean surface with fixed sea surface temperature (SST)
	LEAF-3 (Walko et al. 2000)
Boundary conditions	Periodic in zonal and meridional directions
Microphysics scheme	Two-moment bulk microphysics (Meyers et al. 1997)
	Eight hydrometeor classes (Saleeby and Cotton 2004)
	Heterogeneous ice nucleation (DeMott et al. 2010)
Radiation scheme	Two-stream, hydrometeor sensitive (Harrington 1997)
	Updated every 5 min
Aerosol treatment	Ammonium sulfate aerosol, with single lognormal mode
	Maximum concentration (CCN: 500 mg^{-1}; IN: 0.01 mg^{-1}) at the surface and exponentially decreasing with altitude
	Aerosol–radiation interactions on
	Aerosol sources and sinks on, with full aerosol budget tracking (Saleeby and van den Heever 2013)

Individual congestus updrafts are identified using Tracking and Object-Based Analysis of Clouds (*tobac*), a recently developed tracking algorithm that allows for the offline identification of updraft features and associated condensate volumes (Heikenfeld et al. 2019). First, two-dimensional updraft "features" are identified at each analysis time step ($\Delta t = 5$ min) using the maximum vertical velocity between 2 and 7 km in each column. For clarity, "features" are used in this paper to describe an updraft or cloudy region at one time step, while "cells" refer to a set of updraft or cloudy features tracked as connected in time. These features are identified at multiple threshold values (1, 3, 5, and 10 m s^{-1}), and an area-weighted centroid is assigned to each feature. Second, contiguous regions of cloudy grid cells are identified and, if possible, associated with a given updraft feature using a watershedding technique. A check is done to ensure that the updraft maximum is actually located within the cloudy region, and any other cloudy cells in the column that are not contiguous with the updraft maximum are excluded. From these cloudy points, the contiguous updraft region (with positive vertical velocity) is selected. Third, identified updraft features are linked in time by matching up features in previous time steps with nearby
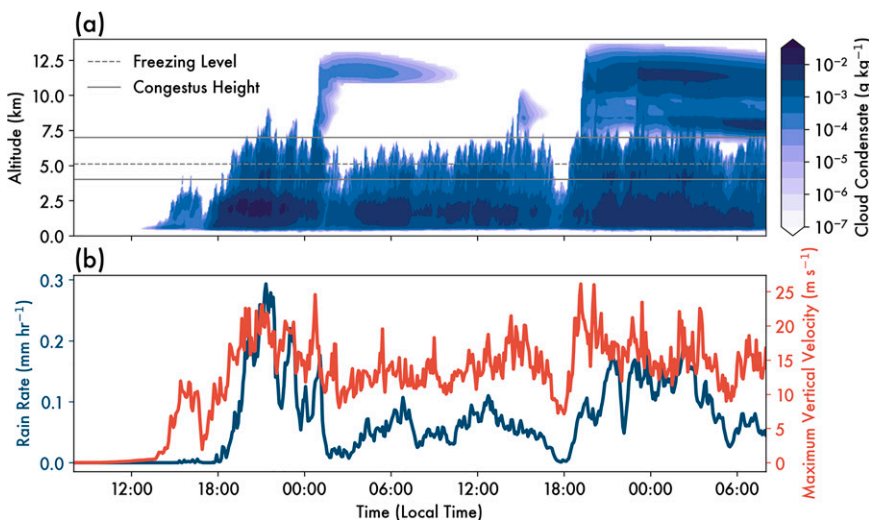

FIG. 2. Mean evolution of the trimodal convective cloud development over the course of the simulation, showing (a) domain-mean cloud condensate (g kg^{-1}) and (b) mean precipitation rate (mm h^{-1}) (blue) and maximum updraft velocity (m s^{-1}) (red). In (a), the 0°C level is indicated by the dashed black horizontal line, and congestus height criteria (4–7 km AGL) are indicated by the solid gray horizontal lines. The simulation began at 0000 UTC (0800 LT). The first 7.5 h of the simulation are considered spin-up time and are not included in the figure or the analysis.
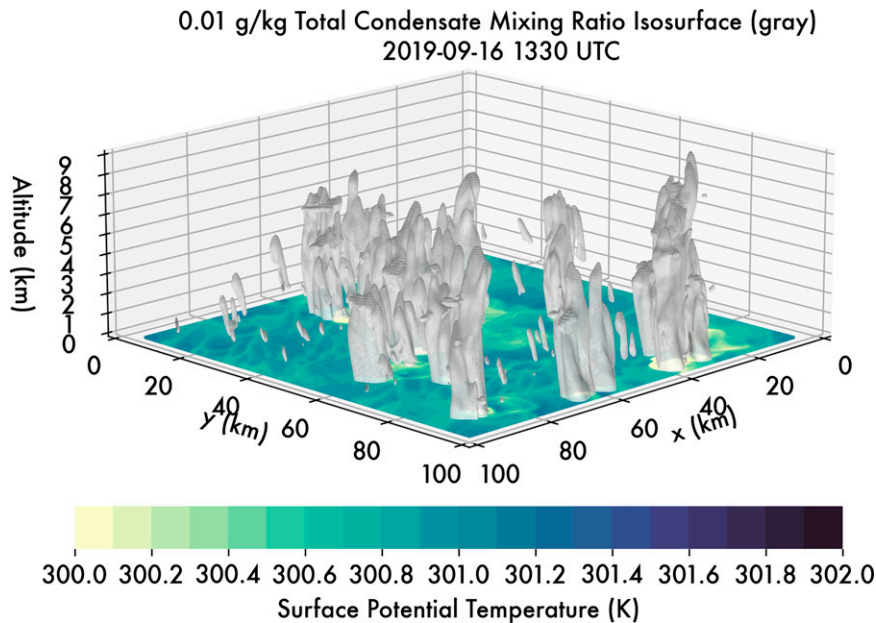
FIG. 3. Three-dimensional snapshot of the cumulus and congestus cloud field at 1330 UTC (2130 LT). Gray isosurfaces are 0.01 g kg^{-1} of cloud condensate. Surface colors are the potential temperature at the lowest above-surface model level and show the development of cold pools in association with the congestus.

features in subsequent time steps based on the predicted updraft motion to create trajectories of tracked "cells." Any features that are not linked to a trajectory or have a lifetime of less than 5 min (i.e., is not identified in at least two consecutive time steps) are excluded from the analysis as a quality check.

Because *tobac* allows updrafts to be tracked in time, we can determine cloud statistics at each time step and over the lifetime of the updraft. Cloud-top height is identified for each feature as the maximum altitude where cloud condensate is greater than 0.01 g kg^{-1}, and cloud-base height is similarly identified as the minimum altitude where cloud condensate reaches the threshold. For each cell trajectory, a maximum CTH is also identified from the feature CTHs at each time step. We define congestus updrafts in this paper as cells which have 1) a cloud base at each time step below 2 km thereby excluding midlevel clouds, such as altocumulus, which have a much shallower vertical extent; 2) a maximum CTH over all time steps between 4 and 7 km; and 3) no other clouds located within the same column for at least 1 km above cloud top or below cloud base at any time step. These requirements are very similar to past studies (Sheffield et al. 2015).

It is important to note that congestus at the very beginning or very end of their life cycle, when their updrafts are weaker than 1 m s^{-1}, are excluded from the analysis. The tracking algorithm, as with most tracking algorithms, requires a physically informed threshold to be set as a minimum for detecting updrafts, and thus this limitation in terms of capturing the full updraft life cycle would be present for any variable used for tracking. However, due to the multiple threshold capabilities of *tobac*, we are able to set a fairly low minimum threshold which we believe allows us to capture a vast majority of the congestus lifetime.

d. Defining terminal and transient congestus

In Luo et al. (2009), terminal and transient congestus are defined based on whether they are negatively or positively buoyant at the time of observation, and hence as to whether they will continue to vertically develop. Although we adopt the terminology *transient* and *terminal*, we use a modified definition in this paper since we are interested in whether a given congestus cloud is capped by the 0°C stable layer.

For each tracked cell, if an identified congestus updraft belongs to a cloud with a maximum CTH between 4 km and the 0°C level (~5.1 km for this simulation) throughout its tracked lifetime, it is considered *terminal*. If the maximum CTH reached over the cloud lifetime is between the 0°C level and 7 km, it is considered *transient*. Transient congestus are further subdivided at each time step into *developing transient* and *mature transient*, based on the CTH assessed at the time step in question. Although both developing and mature transient congestus eventually reach above the 0°C level at some point in their lifetime, *developing transient* are those with a CTH below the 0°C level during a given time step, while *mature transient* are those with a CTH above it. This allows us to compare congestus before they reach the 0°C level to see what differentiates those that are capped or constrained (i.e., terminal) from those that continue to develop vertically (i.e., developing transient). There were very few updrafts which extended above 7 km, but when identified, these were considered as deep convection and excluded from our analysis.

In this work, we track congestus and classify them as terminal or transient based on CTH at 5-min output resolution. It is possible that a congestus may reach a greater CTH than the identified maximum CTH at some time in between sampling;
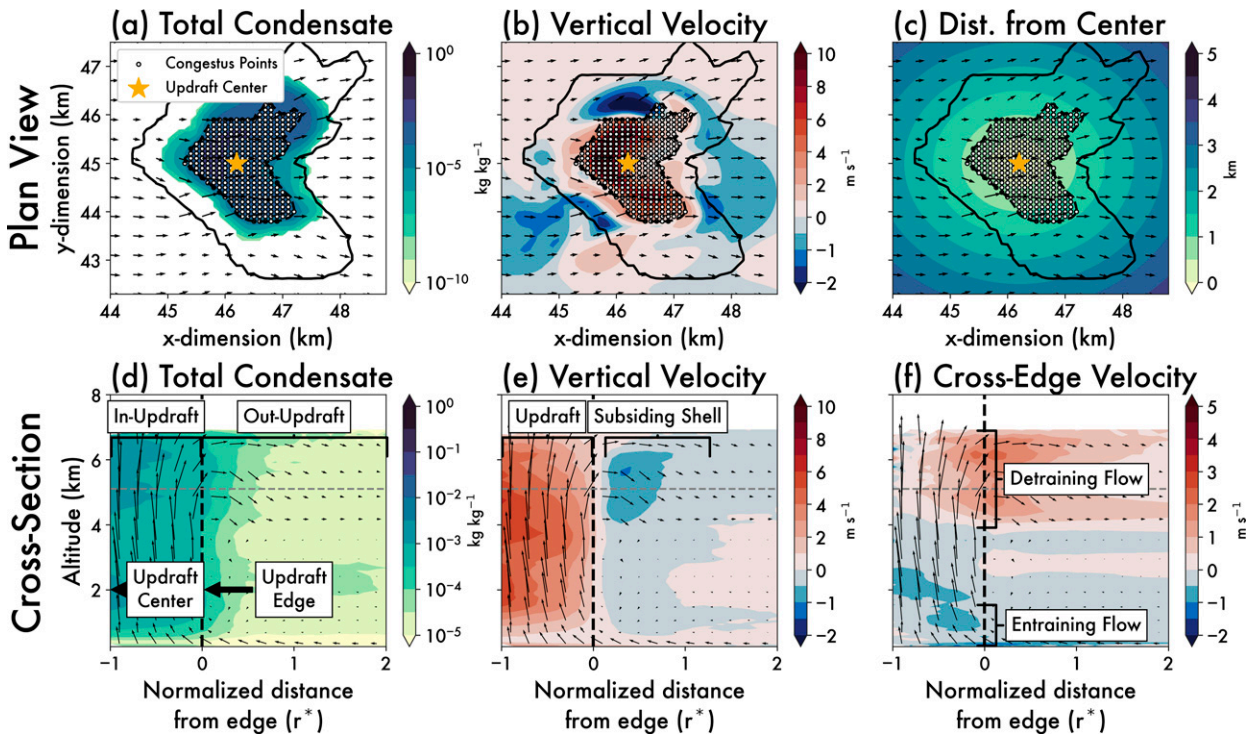
FIG. 4. Definition of the normalized radial coordinates and composite cross sections. (a)–(c) A plan view of a single updraft, where the yellow star is the updraft center, and small black dots represent congestus updraft points as identified by the criteria described in text. Dashed gray contours are the updraft edge ($r^* = 0$) and solid contours are one radius away ($r^* = 1$) from the updraft edge. Horizontal wind barbs are also displayed. (d)–(f) A composite cross section through all congestus updrafts as a function of altitude and normalized distance from the updraft edge ($r^* = 0$), with key aspects of the overall flow annotated. The vertical dashed black line is the updraft edge. The horizontal dashed gray line is the mean 0°C level. Vertical and cross-edge wind barbs are displayed. Note that the color scales for total condensate in (a) and (d) are different.

in this case, this would potentially blur the classification between congestus subcategories. However, this is most likely to happen around the tallest terminal congestus (e.g., when a terminal congestus close to the 0°C level does actually ascend above it for less than 5 min in between analysis times). Since the development only persists briefly, it is unlikely to significantly impact the general results.

e. Compositing approach

Once congestus clouds are identified and classified as terminal or transient, they are aligned in space to generate composites of various fields for each type of congestus. This process is illustrated in Fig. 4. For each congestus updraft, a given field $\psi(x, y, z)$ is redefined relative to the updraft core, defined as the centroid of updraft points at each vertical level weighted by the updraft velocity, to give a transformed field $\psi(r, \theta, z)$. Normalized coordinates are used in the radial direction, and physical coordinates are used in the vertical (Drager et al. 2020). The radial distance r is normalized by the updraft radius $r'(\theta, z)$, which is a function of altitude and azimuthal angle, to give $r^* = r/r' - 1$, such that $r^* < 0$ inside the updraft, $r^* = 0$ at the updraft edge, and $r^* > 0$ outside the updraft (Figs. 4a–d).

Similar to previous analyses, an azimuthal average is taken to yield a composite field in the radial direction (Sherwood

et al. 2013; Romps and Charn 2015; Peters et al. 2019; Savre 2021). The normalized composites allow for an investigation into general updraft structure without "smearing" the features by averaging updrafts of different widths. On the other hand, using physical coordinates for the vertical dimension is useful to compare how dynamic and microphysical fields differ at fixed altitudes (e.g., the 0°C level). Such vertical composites are shown in Figs. 4d–f. Key regions within the updraft referred to within the text (e.g., updraft shell, updraft core, entrainment/detrainment regions) are annotated in Figs. 4d–f to assist in orientating the reader, while a more detailed description of these features can be found in section 4b.

3. Congestus characteristics

In this section, bulk characteristics of the congestus field and differences among transient and terminal congestus are explored. A total of 1552 congestus updraft features comprising 445 tracked cells are observed (Fig. 5a). The CTH distributions (Figs. 5b,c) show a clear peak between 4 and 7 km, which supports the definition of congestus clouds used in this paper. The dashed horizontal line representing the mean 0°C level also separates the congestus distribution into two populations (terminal and transient). Terminal
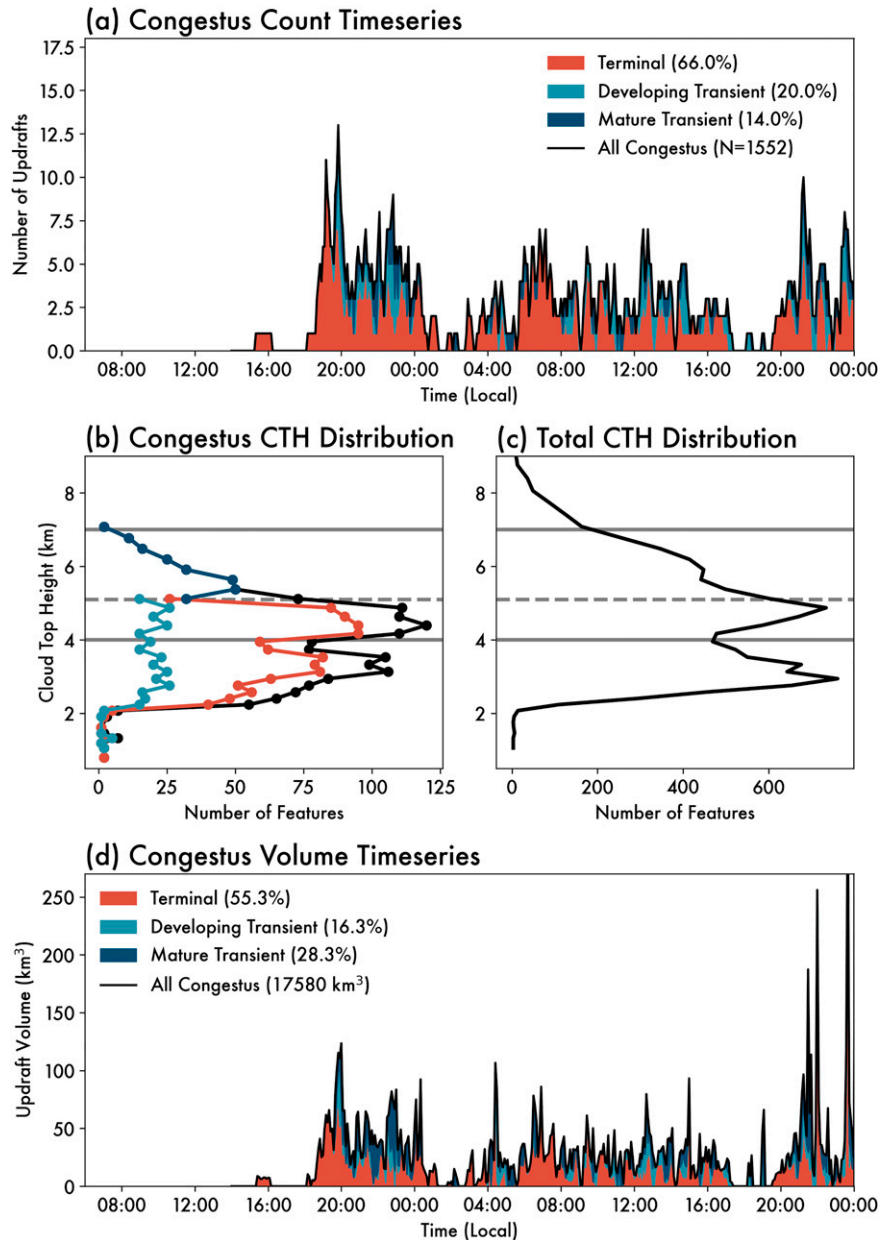
FIG. 5. The characteristics of the congestus in this study as shown by (a) a time series of the number of identified congestus updrafts separated into terminal (red), developing transient (light blue), and mature transient (dark blue) clouds. The colored regions show the relative contributions of each category to the total number of congestus (black line). Histograms of (b) congestus cloud-top heights at each time step and (c) full cloud-top height distribution over entire analysis period, with colors in (b) corresponding to the categories shown in (a). (d) A time series of the total volume occupied by each type of updraft. The 0°C level is indicated by the dashed gray horizontal line, and congestus height criteria (4–7 km AGL) are indicated by the solid gray horizontal lines.

congestus make up 66.0% of tracked cells (Fig. 5a). The other 34.0% of congestus updrafts reach above the 0°C level for at least one time step during their tracked lifetime, with 14.0% of those extending above the 0°C level in the current time step, and hence considered as mature transient congestus.

The proportion of transient congestus to the total number of congestus observed over the entire simulation is similar to the 30%–40% of positively buoyant congestus that Luo et al. (2009) observed using *CloudSat* overpasses, though the definitions of terminal and transient congestus here are different than those in Luo et al. (2009). That being said, the fraction of
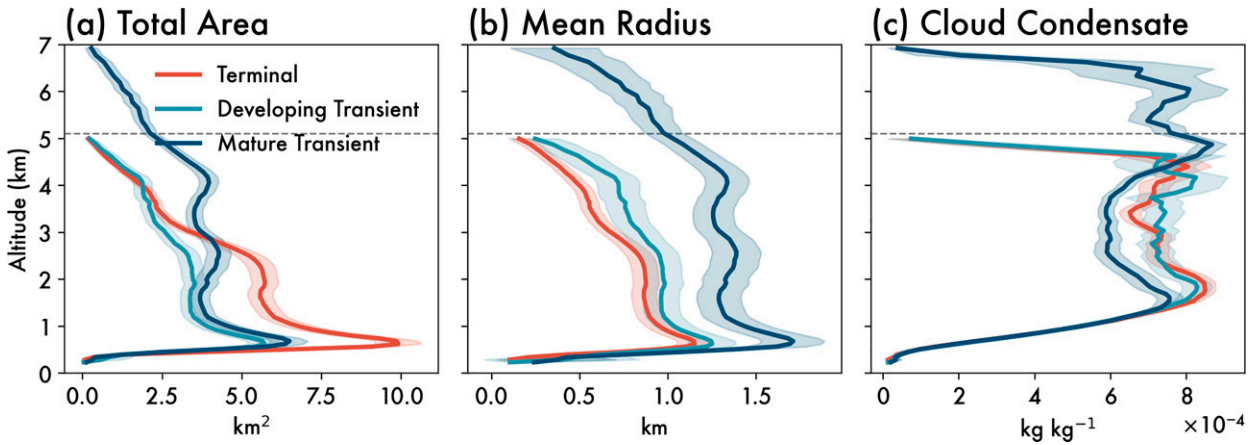
FIG. 6. (a) Total area occupied (km^2), (b) mean effective updraft radius (km), and (c) mean cloud condensate (kg kg^{-1}) for terminal (red), developing transient (light blue), and mature transient (dark blue) congestus. Solid lines are the mean and the shaded areas are the 5%–95% confidence intervals at each vertical level.

congestus considered transient does vary over the course of the simulation.

Despite there being a greater number of terminal congestus updrafts over the simulation period (Fig. 5a), transient congestus updrafts occupy a similar volume overall to the terminal congestus updrafts (Fig. 5d). In terms of mean updraft size, Fig. 6b indicates that the mature transient congestus are the largest at all vertical levels. For congestus below the 0°C level, terminal and developing transient updrafts having have similar radii below 2 km, but developing transient congestus (light blue lines in Fig. 6b) begin to have wider updrafts above 3 km. That being said, because there are more numerous terminal congestus, they occupy a larger total area for vertical levels below 3 km (Fig. 6a). Although developing transient and terminal congestus updrafts have similar cloud-top heights, those that will grow above the 0°C level (i.e., developing transient) tend to be wider close to the cloud top.

The overall structure of congestus updraft velocities is fairly consistent (Fig. 7). The fluctuations in updraft velocity coincide with stable layers in the domain (Fig. 1): updrafts slow down as they ascend through the trade wind stable layer between 2 and 3 km and then again at the 0°C level stable layer between 4 and 5.1 km (dashed gray line in Fig. 7). Differences between terminal and developing transient congestus updrafts become clear above 2.7 km (solid gray line in Fig. 7), with developing transient congestus updraft velocities being stronger thereby allowing them to ascend through the 0°C stable layer. Transient congestus continue to have faster updraft velocities until reaching maturity (Fig. 7e). This increased updraft velocity enhances the ability of transient congestus to reach higher altitudes, impact the midlevel environment around the 0°C level, and thus potentially support the transition into deep convection.

4. Vertical acceleration budget

a. Vertical acceleration calculation

In the next few sections, we investigate the physical processes driving the differences in terminal and transient congestus based on the vertical acceleration budgets. The conditionally sampled vertical momentum equation can be written in the following form, and is similar to de Roode et al. (2012) and many cumulus parameterizations:

$$
\underbrace{\frac{\partial w_c}{\partial t}}_{\text{time tendency}} = \underbrace{B_c}_{\text{Term 1: buoyancy}} + \underbrace{-\frac{1}{\lfloor\rho\rfloor_c}\left\lfloor\frac{\partial p'}{\partial z}\right\rfloor_c}_{\text{Term 2: perturbation pressure gradient}}
$$

$$
+ \underbrace{-\frac{1}{A_c\lfloor\rho\rfloor_c}\oint_c \boldsymbol{v}_H \cdot \hat{\mathbf{n}}(w - w_c)\rho dC}_{\text{Term 3: momentum entrainment}}
$$

$$
+ \underbrace{-\frac{1}{2}\frac{\partial w_c^2}{\partial z}}_{\text{Term 4: vertical advection}} + \underbrace{-\frac{1}{A_c\lfloor\rho\rfloor_c}\frac{\partial A\lfloor\rho(w - w_c)\rfloor_c^2}{\partial z}}_{\text{Term 5: turbulent vertical flux}}
$$

$$(1)$$

where we sample only cloudy updraft points or some subset of those points (e.g., only terminal congestus updrafts). At each vertical level, the conditionally sampled area is A_c. The conditional average is represented by the $\lfloor\rfloor_c$ operator, such that $\lfloor\psi\rfloor_c = (\int_c\psi dC)/A_c$. Similarly, terms with a subscript ψ_c are density-weighted conditional averages such that $\psi_c = (\int_c\rho\psi dC)/(A_c\rho_c)$, where ρ is the density. The full derivation of Eq. (1), is shown in the appendix. The term on the left-hand side of Eq. (1) is the time tendency of updraft velocity w for a given time step at each vertical level. The terms on the right-hand side represent forcings that drive the vertical acceleration. The first term is the acceleration due to buoyancy $[B = g(\theta'/\theta_0) + gr_v'(1 - \epsilon)/\epsilon - gr_c]$, where g is the gravitational acceleration, θ is potential temperature, r_v is the water vapor mixing ratio, and r_c is the total condensate mixing ratio; specifically, this can be broken down into buoyancy due to thermal perturbations $[g(\theta'/\theta_0)]$, water vapor mixing ratio perturbations $[gr_v'(1 - \epsilon)/\epsilon]$, and condensate loading $(-gr_c)$. The second term is the acceleration due to the PPGF, where p is the pressure. The third term is entrainment of vertical momentum into/out of the conditionally sampled area (where $\boldsymbol{v}_H$
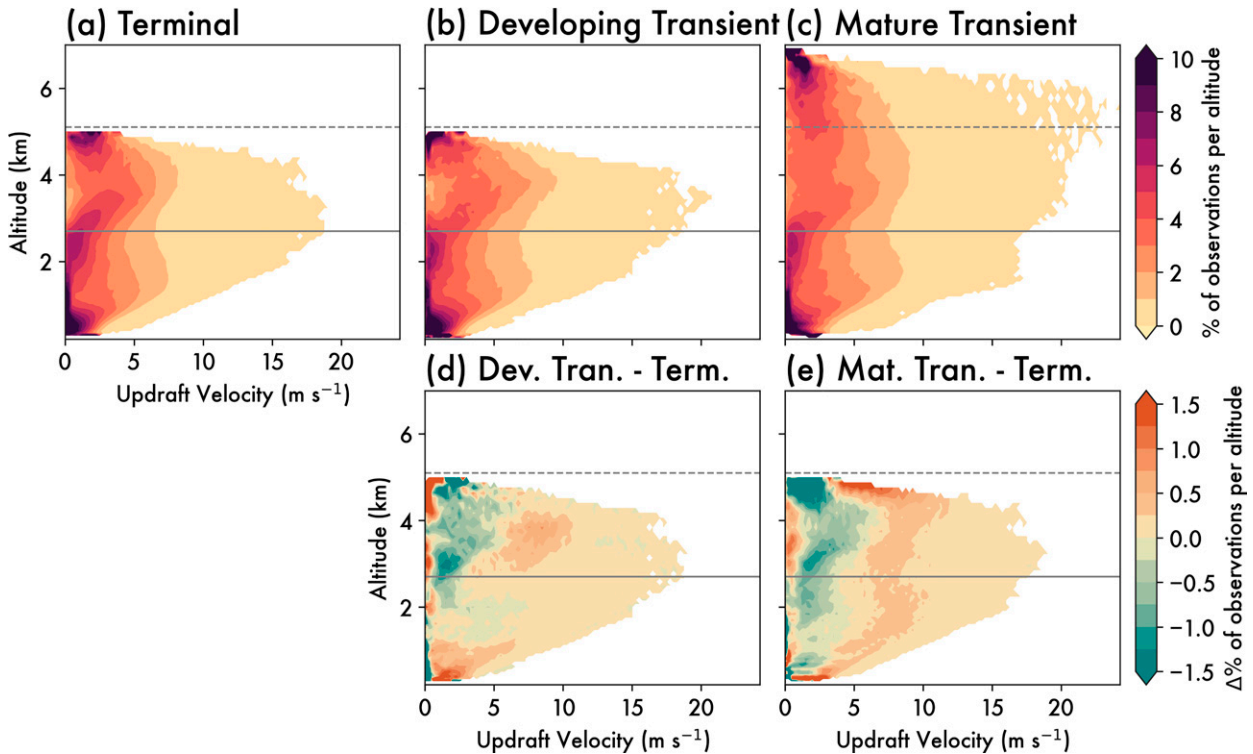
FIG. 7. Contoured frequency by altitude diagrams (CFADs) of updraft velocity (m s^{-1}) as a function of altitude (km), for (a) terminal, (b) developing transient, and (c) mature transient congestus. (d),(e) The difference in percent of the developing and mature transient congestus relative to terminal congestus. Note that altitudes above 5.1 km in (d) and (e) have been left blank because there are no terminal congestus above that altitude, as defined in text. The horizontal dashed gray line indicates the mean 0°C level, and the solid gray line indicates 2.7 km AGL as discussed in text.

is the horizontal wind vector), and the last two terms are the bulk and turbulent advection of vertical momentum, respectively.

The prime (′) on the terms in Eq. (1) denotes a perturbation calculated relative to an environmental base state (denoted by a subscript zero). We follow a similar approach to Marinescu et al. (2021) in calculating the base state. At each time step, the median of all noncloudy grid points (condensate < 0.01 g kg^{-1}) is taken at each model altitude thus comprising the environmental profile from which to calculate perturbations at each time step. We use the median of noncloudy grid points rather than the temporally invariant model base state, but the two are in good agreement and differ only marginally. It should be noted that at each time step, the perturbation is taken from a single background profile rather than relative to the nearby environment of each updraft for the sake of simplifying computations, though this may cause some deviation from the actual acceleration experienced by an updraft (Davies-Jones 2003; Peters 2016).

b. Composite vertical profiles

Mean vertical profiles of the terms driving the vertical velocity for each congestus type are shown in Fig. 8. Over the whole congestus ensemble, buoyancy and PPGF (Figs. 8b,c) have the largest magnitudes, which is consistent with many past studies of updraft momentum budgets (e.g., de Roode et al. 2012). Buoyancy and PPGF have approximately opposite trends with a slight offset in the vertical such that the PPGF acts as a drag on the buoyancy acceleration. The horizontal entrainment of momentum is close to zero (Fig. 8e). Turbulence and vertical advection of momentum (Figs. 8f,g) generally have smaller magnitudes than buoyancy and PPGF throughout the column, but have appreciable magnitudes nearing the 0°C level and above.

Although buoyancy and PPGF account for the largest magnitudes of updraft acceleration, their sum does not fully describe the shape of the vertical velocity profile. Positive net accelerations would generally lead to increases in vertical velocity with height, with the opposite for negative accelerations. The combination of buoyancy and PPGF (Fig. 8d) does not match up with the turning points in the vertical velocity profile (Fig. 8a), which are drawn as gray lines to guide the reader. Instead, accounting for the acceleration due to vertical advection (both bulk advection in Fig. 8g and subplume fluctuations in Fig. 8f) leads to a better alignment with the mean updraft profile (Fig. 8h).

As shown previously, mature transient congestus have stronger updrafts than terminal congestus all throughout the column (Fig. 8a). On the other hand, developing transient congestus only have stronger updrafts than terminal congestus
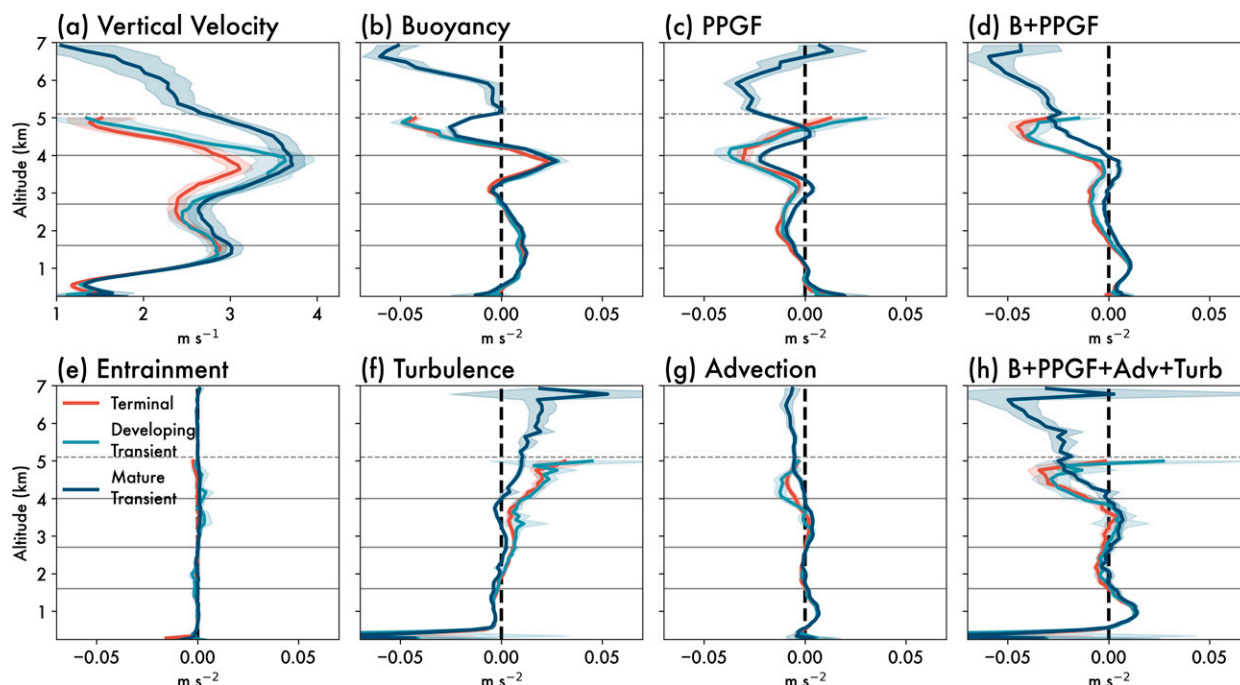
FIG. 8. Profiles of vertical velocity and the terms primarily contributing to the updraft acceleration for terminal (red), developing transient (light blue), and mature transient (dark blue) congestus. Lines represent mean vertical profiles of (a) vertical velocity (m s^{-1}), (b) buoyancy acceleration, (c) PPGF acceleration, (d) the sum of buoyancy and PPGF accelerations, (e) horizontal entrainment acceleration, (f) turbulent vertical advective acceleration, (g) bulk vertical advective acceleration, and (h) the sum of buoyancy, PPGF acceleration, turbulent, and vertical advective acceleration (all in m s^{-2}), as a function of altitude (km). Shaded areas cover the 5%–95% confidence intervals at each level. The horizontal dashed line denotes the mean 0°C level, while the horizontal solid lines correspond to levels where the first derivative of vertical velocity changes sign.

above 2.7 km AGL (Fig. 9a). This increase in developing transient updraft velocity occurs alongside an increase in buoyancy relative to terminal congestus (especially thermal buoyancy, as shown in Figs. 9b,c). This adds support to earlier findings that environments favoring more buoyant updrafts tend to produce more transient congestus (Redelsperger et al. 2002; Takemi et al. 2004; Jensen and Del Genio 2006). Although a combination of acceleration terms is needed to fully describe the shape of the vertical velocity profile, buoyancy is the primary driver of those congestus which are able to ascend through the 0°C level.

c. Composite cross sections

We have shown that directly below the 0°C level, transient congestus tend to be more buoyant than terminal congestus, which allows them to continue developing vertically through the 0°C stable layer. To improve our physical understanding as to why this is the case, we construct combined vertical and radial composites to examine the horizontal structure of the updraft and its interactions with the surrounding environment.

Figure 10 shows composite cross sections of total condensate, vertical velocity, cross-cloud edge velocity, and latent heat released as a result of vapor to liquid transitions for terminal, developing transient, and mature transient updrafts. The vertical axis corresponds to altitude. The horizontal axis represents normalized distance from the cloud edge, with the cloud edge located at $r^* = 0$ (black dashed line), the in-cloud

points located to the left of $r^* = 0$ (black dashed line), and the environmental points to the right of $r^* = 0$. Wind barbs show the mean circulation through the updraft. It is evident that updraft velocity and condensate tend to decrease moving radially outwards from the center (Figs. 9a–f), which is consistent with a switch from net latent heat release within the updraft core arising from condensation and cloud droplet activation (warm colors in Figs. 10j–l), to net latent heat absorption outside the updraft due to evaporation (cool colors in Figs. 10j–l).

Directly surrounding the updraft, there is a shell of subsiding air that is narrower than the updraft itself (Figs. 10d–f). The strongest downdrafts occur just below the level of cloud top, at the altitude of maximum updraft velocity, a feature also observed by Savre (2021). The shape of the subsiding shell is consistent with vortex dynamics and numerous other studies focused on such effects (Sherwood et al. 2013; Romps and Charn 2015; Peters et al. 2019; Savre 2021). The composite wind field shows the updraft and downdraft as part of a circulation with entrainment near cloud base and detrainment toward cloud top (Figs. 10g–i). Closer to the updraft core, mean winds are directed toward the updraft core as high ~3–4 km AGL.

Overall, mature transient congestus have faster updraft velocities (Figs. 10d,f) and more condensate mass (Figs. 10a,c) than terminal congestus. The differing height relative to the
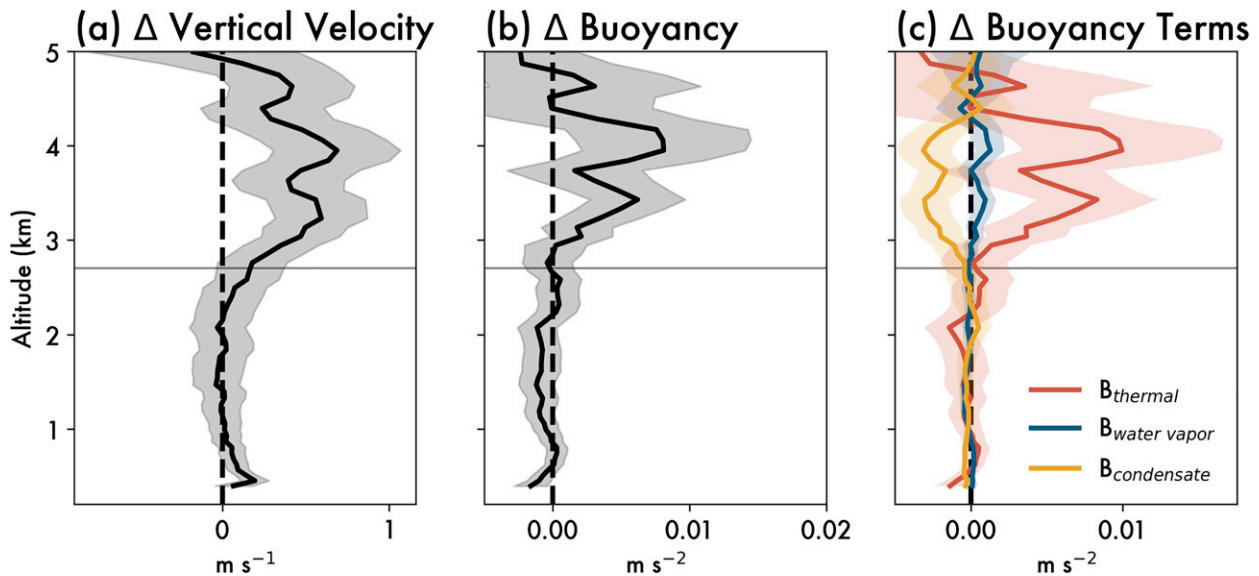
FIG. 9. Difference profiles of developing transient and terminal congestus in terms of (a) vertical velocity (m s^{-1}), (b) buoyancy (m s^{-2}), and (c) individual buoyancy terms (m s^{-2}). Shaded areas cover the 5%–95% confidence intervals at each level. Horizontal solid gray line indicates 2.7 km AGL, as described in text.

0°C level also strongly impacts the subsiding shell. Terminal congestus downdraft shells are more column shaped, extending fairly continuously until close to cloud base (Fig. 10d). Mature transient congestus have more of a vortex-driven structure, with a strong downdraft at cloud-top height to just above the 0°C level and weaker downdrafts below. The updraft circulation is broken up by the stable layer to form distinct circulations above and below the 0°C level (Fig. 10i). Similar large-scale circulations around the 0°C level were also seen in Posselt et al. (2008).

To further investigate why terminal congestus tend to be less buoyant than developing transient congestus above 2.7 km AGL (as shown in Fig. 9), and thus why developing transient congestus are ultimately able to extend past the 0°C level, we compare their cross sections of various properties in Fig. 11. Looking at these cross sections allows us to identify differences not only within the updraft, but also between the environments in which the two types of congestus develop.

Transient congestus tend to develop in more humid environments ($r^* > 2$ in Fig. 11c), particularly above ~2 km AGL. At corresponding altitudes, terminal congestus experience more evaporation of cloud droplets (Fig. 11f) alongside a drop in buoyancy relative to transient congestus (Figs. 9b,c). This suggests that transient congestus are more protected from dilution in the midlevels between ~3 km AGL and the 0°C level, explaining their faster updraft velocities in this region (Fig. 9a). Transient congestus updrafts are mixed with more humid environmental air, leading to less droplet evaporation and greater buoyancy compared to terminal congestus at the same altitudes. The importance of humidity between the trade wind and 0°C level stable layers supports previous research (e.g., Redelsperger et al. 2002) that found midlevel dry layers to be the most important environmental factor determining congestus height.

This effect is compounded by transient congestus being wider than terminal congestus at those altitudes (Fig. 6b), which further protects their updraft cores from dilution. The difference in equivalent potential temperature (θ_e) is shown in Figs. 11j–l as a metric for dilution, with larger θ_e values correspond to air originating from the surface, and decreases in θ_e from cloud base to cloud top being reflective of environmental air mixing into the updrafts. Comparing the terminal and developing transient congestus shows that terminal congestus tend to be more diluted (Fig. 11l), particularly above ~2.7 km where the substantial differences in updraft width contribute to differences in buoyancy dilution and thereby overall vertical momentum.

The increase in updraft velocities below the 0°C level allows developing transient congestus to activate and maintain more cloud condensate as they encounter the 0°C stable layer (Figs. 11i and 6c). As mature transient congestus cross the 0°C level, they do still experience a dip in buoyancy as a result of the increased condensate loading and the decreased thermal buoyancy (dark blue line in Fig. 8b). However, upon crossing the 0°C level, the condensate can start to freeze and release latent heat (Fig. 10o), which allows them to regain some buoyancy (Fig. 8b) and continue developing vertically.

5. Aerosol activation and detrainment

The differences in vertical development between terminal and transient congestus as discussed in section 4 lead to differences in cloud-top height relative to the 0°C level. In this section, we examine the effects of those differences on the convective transport of water vapor and aerosol particles. RAMS aerosol budget capabilities (Saleeby and van den Heever 2013) allow us to track how aerosol particles within the model domain interact with, and are redistributed by, congestus updrafts. Figure 12 shows composites of water vapor and
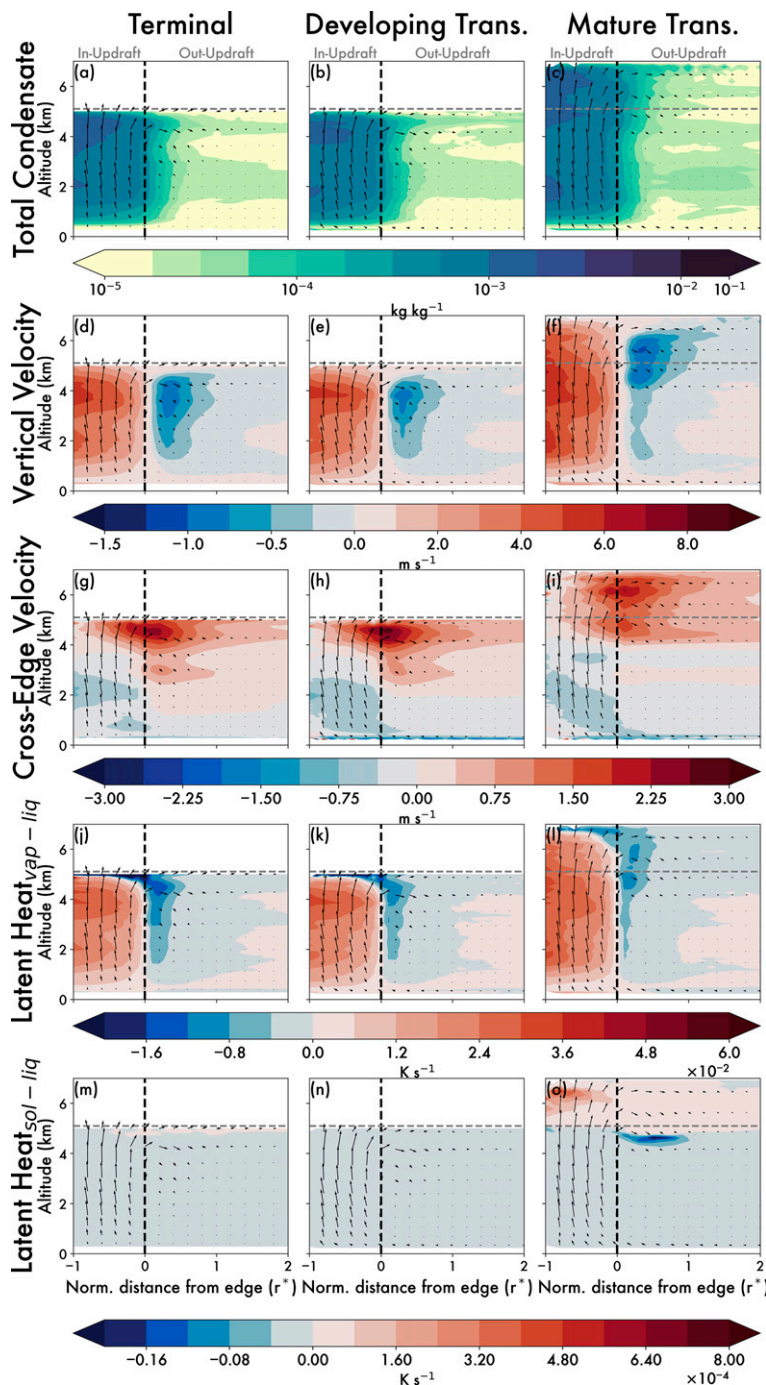
FIG. 10. Composite congestus updraft cross sections of (a)–(c) total condensate (kg kg^{-1}), (d)–(f) vertical velocity (m s^{-1}), (g)–(i) cross-edge velocity (m s^{-1}), (j)–(l) latent heat due to vapor–liquid transitions (K s^{-1}), and (m)–(o) latent heat due to solid–liquid transitions (K s^{-1}) as a function of the normalized distance from core edge (r^*) and altitude. (left) A composite of terminal congestus, (center) a composite of developing transient congestus, and (right) a composite of mature transient congestus. The wind barbs show mean vertical and cross-edge flow relative to clear-sky conditions. The black vertical dashed line at $r^* = 0$ denotes the mean edge of the updraft. Only coordinates with more than 50 samples are shown. Areas above 5.1 km AGL are left blank in the left and center columns since terminal congestus and developing transient congestus are defined to have cloud tops below the 0°C level (denoted by the horizontal dashed gray line).
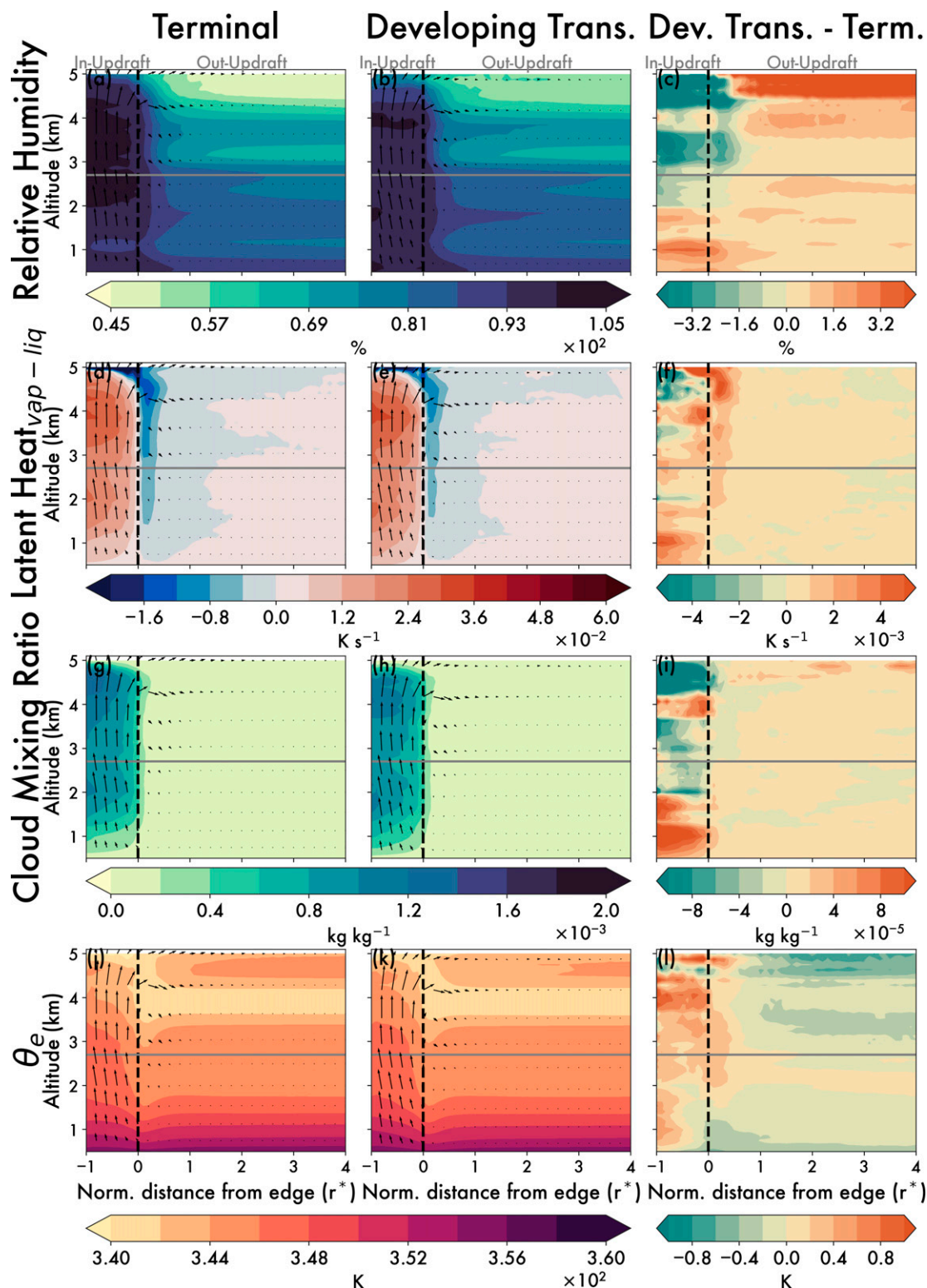
FIG. 11. As in Fig. 10, but comparing the development of terminal and developing transient congestus in terms of (a)–(c) relative humidity (%), (d)–(f) latent heat from vapor–liquid transitions (K s^{-1}), (g)–(i) cloud mixing ratio (kg kg^{-1}), and (j)–(l) equivalent potential temperature (K). Only altitudes up to 5.1 km AGL are shown since only terminal and developing transient congestus are depicted. The horizontal solid gray line denotes an altitude of 2.7 km AGL as described in text.
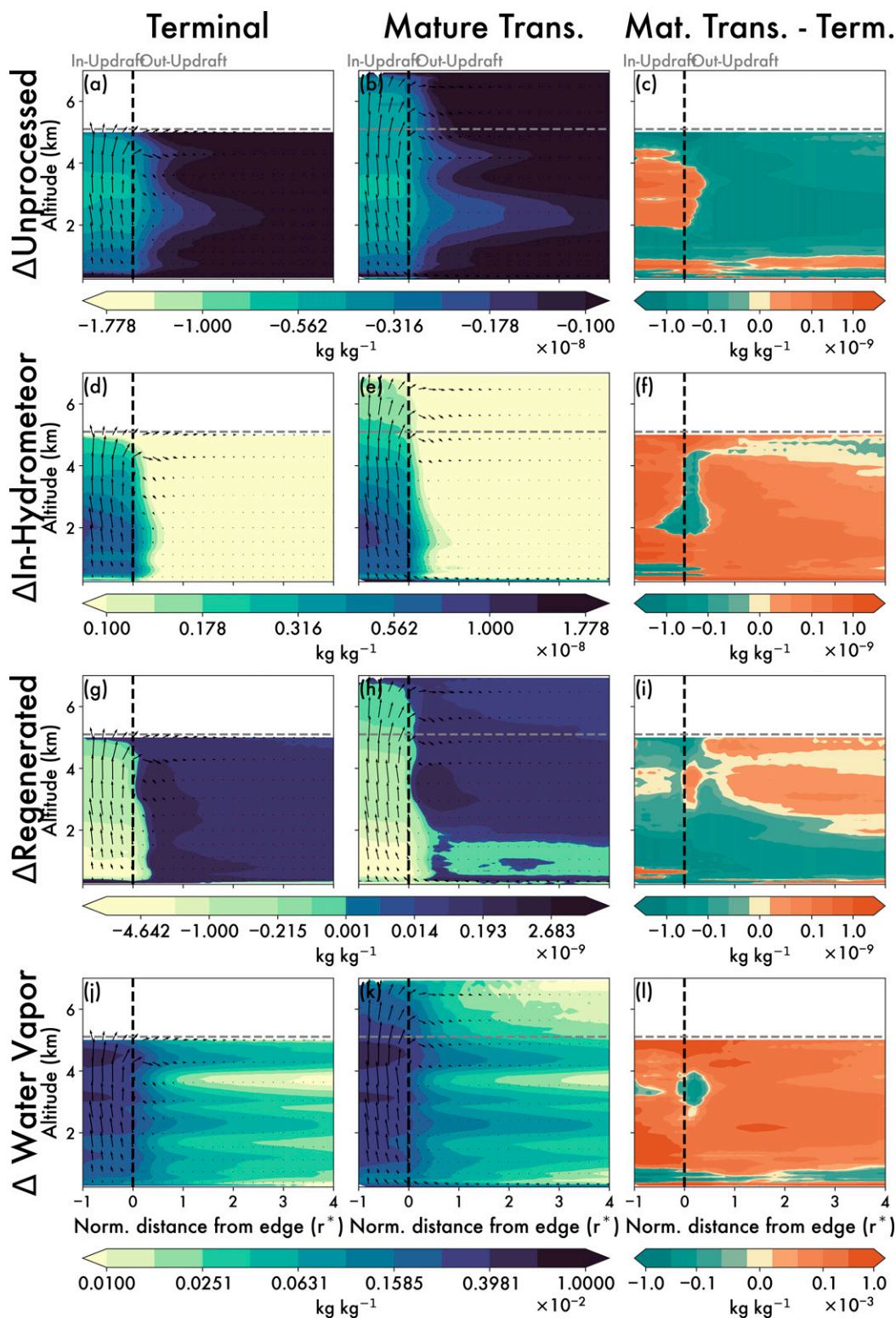
FIG. 12. As in Fig. 11, but for the aerosol budget terms described in the text (kg kg^{-1}), as well as the water vapor enhancements (kg kg^{-1}). Enhancements are taken relative to clear-sky profiles at each time step. (left) A composite of terminal congestus, (center) a composite of mature transient congestus, and (right) the difference between the center and left columns. Areas above 5.1 km in the difference plot are left blank since terminal congestus are defined to have tops below 5.1 km. The gray dashed line indicates the mean 0°C level.

three separately tracked terms within the aerosol budget taken as perturbations from the clear-sky mean at the same time step. Aerosol particles are initialized in the *unprocessed* aerosol term. When they are activated as CCN in cloud droplets, the aerosol mass is transferred to the *in-hydrometeor* aerosol term. As those hydrometeor droplets evaporate under subsaturated conditions, the aerosol mass contained in those droplets is returned to the domain in the *regenerated* aerosol term.

Transient and terminal congestus have similar patterns of the surrounding aerosol fields: unprocessed aerosol concentrations are lower around and within congestus updrafts, as those aerosol particles are activated as CCN and are subsequently transferred to the in-hydrometeor category. A majority of aerosols enter the updraft at cloud base at the entraining branch of the overturning circulation involving the updraft and its surrounding shell (Figs. 12a,b). For transient congestus though, which extend above the 0°C level, the overturning circulation is broken into two circulations, one above and one below the 0°C stable level (Figs. 10f,i). As a result, there is also entrainment into the updraft at the 0°C level for mature transient congestus (Fig. 12b). This entrainment of aerosol particles around stable layers has implications for what air masses are entrained into clouds, especially in regions with vertical inhomogeneity in aerosol or water vapor concentrations.

Once the aerosol enters the updraft, it activates cloud droplets and enters the in-hydrometeor aerosol category (Figs. 12d,e). Most aerosol particles are activated within 2 km above cloud base, with more being activated toward the center of the updraft, where updraft velocities are highest and the concomitant production in supersaturation is greatest, compared with the outer regions of the updraft. Transient congestus activate more aerosol particles than terminal congestus throughout most of the column (Fig. 12f), due to their stronger updraft velocities producing higher supersaturations.

Aerosol particles are regenerated, and returned to the atmosphere, along cloud edges where the updraft is weak and supersaturation is insufficient to activate available CCN and condense water onto existing droplets. Hence, evaporation dominates (Figs. 12g,h). Once the liquid water is evaporated the aerosol particles are returned to the subsaturated environment. As the droplets evaporate, water vapor is also enhanced relative to the clear-sky background (Figs. 12j,k). Most aerosol is regenerated near cloud top and along the edges of the updraft which is in keeping with the fact that these regions of the cloud are more susceptible to dry air entrainment and mixing, and hence evaporation. Around the cloud edges, terminal congestus evaporate more readily (Fig. 11j) upon mixing with their less humid environments (Fig. 11a), compared to transient congestus. As a result, they subsequently release more regenerated aerosol than transient congestus (Fig. 12i).

Transient congestus also regenerate notable aerosol mass within the updraft above the 0°C level (Fig. 12h), despite being buoyant with a positive acceleration at those altitudes (Figs. 8b,g), and an associated net release of latent heat (Fig. 10l). This increase in regeneration may be attributed to reductions in updraft velocity and hence the generation of supersaturation

after penetrating the 0°C stable layer. Regeneration may further be increased in the transition from warm to mixed-phase regions as ice nucleation begins, and liquid water is evaporated and lost to ice through the Wegner–Bergeron–Findeisen process (Verheggen et al. 2007; Engström et al. 2008; Corr et al. 2016). These returned or regenerated aerosol particles are transported outward in the detraining layer, as well as downward in the subsiding shell. This detrainment of aerosol particles lead to enhanced aerosol concentrations as far as two updraft radii away from the updraft edge (~2–4 km away).

Although transient congestus have comparatively stronger downdrafts than terminal congestus at their respective cloud-top heights (Figs. 10d,f), terminal congestus downdrafts extend all the way to cloud base, while mature transient congestus downdrafts are broken up by the 0°C stable layer. *As a result, terminal congestus have greater amounts of regenerated aerosol between the surface and 3 km (Fig. 12i), while transient congestus have greater regenerated aerosol and water vapor in midlevel detrainment layers.* The aerosol and water vapor being detrained above the 0°C stable layer in mature transient congestus clouds are less able to be transported to the surface by virtue of the presence of the stable layer, and a local maximum of aerosol and water vapor is formed around the 0°C level. This has significant implications for subsequent aerosol activation and the formation of cloud droplets in altocumulus clouds. This also emphasizes the role of congestus detrainment in modifying the near-cloud environment, as well as the manner in which the heights of terminal and transient congestus relative to stable layers influence this modification.

6. Discussion and conclusions

Despite the importance of cumulus congestus as a mode of tropical convection, relatively little is understood about what causes some congestus to be capped by the 0°C stable layer (i.e., terminal) while others are able to penetrate the 0°C stable layer and continue to develop vertically (i.e., transient). With the goal of enhancing our scientific understanding of congestus updraft processes, we conducted high-resolution large-eddy simulations of an idealized congestus cloud field and created composites of congestus properties in both the vertical and radial dimensions. The use of *tobac*, an object-tracking algorithm, allowed for updrafts to be tracked in time thereby providing a more accurate comparison of terminal versus transient congestus processes than afforded by domain averages or other bulk analyses.

We first examined the physical mechanisms that govern the updraft acceleration budget of congestus clouds. The balance between buoyancy and perturbation pressure gradient accelerations was shown to describe the shape of the updraft vertical velocity profiles better than either term alone. We also showed that accounting for vertical advection of momentum throughout bulk and turbulent motions improved the representation of the overall vertical velocity profile than simply considering the sum of the buoyancy and PPGF.

We demonstrated that transient congestus have stronger updrafts and higher cloud tops than terminal congestus.
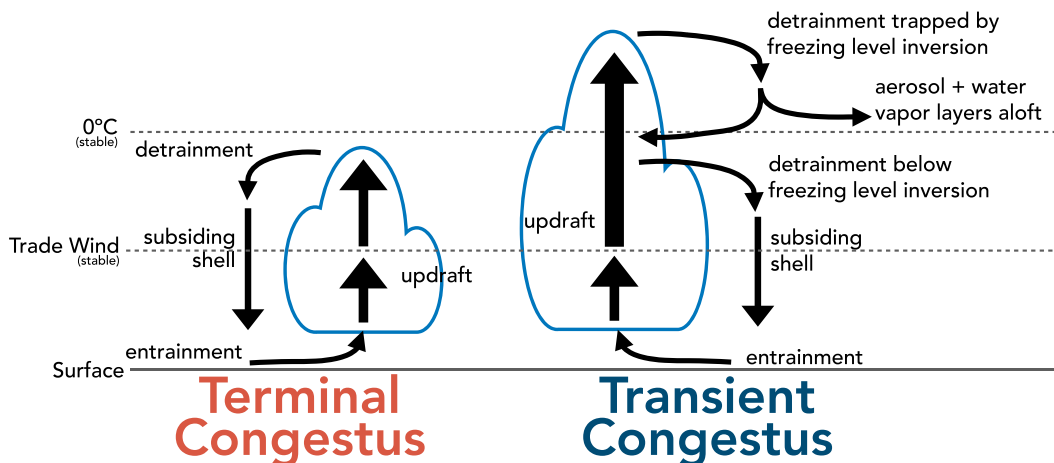
FIG. 13. Schematic representing a conceptual model of the differences in updraft and downdraft circulations and the associated detrainment processes of terminal and transient congestus.

Despite these differences, both types of congestus have similarly structured updrafts characterized by an overturning circulation between the updraft and surrounding subsiding shell. A conceptual schematic depicting the overturning circulations of terminal and transient congestus is shown in Fig. 13. Terminal and transient congestus updrafts are both surrounded by relatively weaker downdrafts, though terminal congestus downdrafts are more vertically homogeneous and extend all the way to cloud base. Transient congestus downdrafts on the other hand have stronger maxima above the 0°C level, and the overturning circulation is broken up into distinct branches separated by the 0°C stable layer in addition to the branches separated by the trade wind stable layer.

In analyzing which factors of the vertical acceleration budget predominantly influenced the differences between the two types of congestus, we have shown that buoyancy is essential for distinguishing between transient and terminal congestus. This supports previous work that found strong correlations between environments favoring more buoyant updrafts and taller congestus (Jensen and Del Genio 2006; Redelsperger et al. 2002). We established a physical mechanism for this process by showing that transient congestus are surrounded by more humid environments above 2.7 km AGL, which corresponds to more protection from evaporation, increased buoyancy, and ultimately increased vertical velocity near the 0°C level relative to terminal congestus.

Finally, aerosol budget tracking and compositing allowed us to describe how detrainment from congestus updrafts influenced their near-cloud environments, including aerosol loading. Transient congestus ingest more aerosols due to their increased updraft velocities. Terminal congestus regenerate more aerosol along their edges due to increased evaporation as a result of their drier environments. However, beyond the subsiding shell, transient congestus have a larger contribution to midlevel aerosol layers, as they detrain aerosols above the 0°C stable layer and rapidly transport it radially outwards, rather than directly toward the surface due to constraints imposed by the 0°C stable layer. By virtue of both

of these different water vapor and aerosol detrainment circulations, the ratio of terminal to transient congestus within an environment therefore has implications for the location and development of midlevel clouds such as altocumulus.

It should be cautioned that the results of this study, while based on a large population of congestus updrafts at varying stages of their life cycle, only describe one tropical maritime environment. The environment influences the vertical structure of the congestus and the proportion of terminal to transient congestus. It would be interesting to utilize the vertical acceleration framework used in this study to examine how the balance between buoyancy, PPGF, and vertical momentum advection changes with environmental properties such as the strength of the 0°C stable layer, midlevel humidity, wind shear, and even the vertical gradient of aerosol concentration. Furthermore, the aerosol composites from this study suggest that environments with differing proportions of transient congestus, as has been shown for increased surface aerosol loadings in Sheffield et al. (2015), are likely to have differences in midlevel aerosol and water vapor detrainment layers. This is an ongoing area of research by the authors, and the results presented in this study will serve as a valuable control simulation to better understand how congestus updrafts vary in differing thermodynamic and aerosol environments.

Data availability statement. The numerical model simulations upon which this study is based, as well as model namelists and information necessary to reproduce the simulation, are available through Mountain Scholar at http://doi.org/10.25675/10217/234037.

APPENDIX

Derivation of the Compressible Vertical Momentum Budget for a Cloud Ensemble

First, the continuity equation can be written in flux form as

$$\frac{\partial \rho}{\partial t} + \boldsymbol{\nabla} \cdot (\rho \mathbf{v}) = 0, \tag{A1}$$

where ρ is the density and $\mathbf{v}$ is the full velocity vector.

Given this, we can define some area of interest c (e.g., congestus updrafts) denoted by an activation function $I(x, y, z, t)$ that is equal to 1 for the region of interest and 0 otherwise. The conditional mean of some field ψ taken only over the area of interest is $[\psi]^c = (1/A_c) \int_c \psi dA = (1/A_c) \int_{\text{domain}} \psi I dA$, where A_c is the area of interest. By Leibniz's rule, conditional averages of derivatives include an extra term as described in Siebesma (1998): $[\partial \psi/\partial z]^c = (1/A_c) \int_c (\partial \psi/\partial z) dA = (1/A_c) [\partial A_c [\psi]^c/\partial z]$. We ignore the boundary terms in Leibniz's rule by defining the conditional area as updrafts such that ψ is constant along the boundaries.

We can then take the conditional average of Eq. (A1) to be

$$\frac{1}{A_c} \frac{\partial A_c [\rho]^c}{\partial t} = -[\boldsymbol{\nabla}_H \cdot (\rho \mathbf{v}_H)]^c - \frac{1}{A_c} \frac{\partial A_c [\rho w]^c}{\partial z}. \tag{A2}$$

For convenience, we define $\rho_c = (\int_{\text{domain}} I \rho dA)/A_c$ to be the conditional average of ρ, and $w_c = \int_{\text{domain}} I \rho w dA / \int_{\text{domain}} I \rho dA = [\rho w]^c/\rho_c$ to be the density-weighted conditional average of the vertical velocity w. Substituting this and using Green's theorem to simplify the divergence term into a closed integral over the conditionally selected area c makes Eq. (A2) equivalent to

$$\frac{1}{A_c} \frac{\partial A_c \rho_c}{\partial t} = -\frac{1}{A_c} \oint_c \mathbf{v}_H \cdot \hat{\mathbf{n}} \rho dC - \frac{1}{A_c} \frac{\partial A_c \rho_c w_c}{\partial z}. \tag{A3}$$

Similarly, the momentum equation can be written as

$$\frac{Dw}{Dt} = \frac{\partial w}{\partial t} + \mathbf{v} \cdot \boldsymbol{\nabla} w = -\frac{1}{\rho} \frac{\partial p'}{\partial z} + B, \tag{A4}$$

where p' is the perturbation from base-state pressure and B is buoyancy.

Combining Eq. (A4) times ρ with Eq. (A1) times w gives

$$\frac{\partial \rho w}{\partial t} + \boldsymbol{\nabla} \cdot (\rho w \mathbf{v}) = -\frac{\rho}{\rho} \frac{\partial p'}{\partial z} + \rho B. \tag{A5}$$

This can be conditionally sampled as above:

$$\frac{1}{A_c} \frac{\partial A_c [\rho w]^c}{\partial t} = -\frac{1}{A_c} \oint_c \mathbf{v}_H \cdot \hat{\mathbf{n}} \rho w dC - \frac{1}{A_c} \frac{\partial A_c [\rho w^2]^c}{\partial z}$$
$$- \left[\frac{\partial p'}{\partial z}\right]^c + [\rho B]^c$$
$$= \frac{1}{A_c} \frac{\partial A_c \rho_c w_c}{\partial t} = \frac{w_c}{A_c} \frac{\partial A_c \rho_c}{\partial t} + \rho_c \frac{\partial w_c}{\partial t}, \tag{A6}$$

where the term $w = w_c + w'$ can be decomposed such that w' is the perturbation from the ensemble value of w_c. Thus, we obtain

$$[\rho w^2]^c = \frac{\int_{\text{domain}} I \rho w^2 dA}{A_c} = \frac{\int_{\text{domain}} I \rho (w_c + w')^2 dA}{A_c}$$
$$= \frac{\int_{\text{domain}} I \rho w_c^2 dA}{A_c} + \frac{\int_{\text{domain}} I \rho w'^2 dA}{A_c}$$
$$= w_c^2 \frac{\int_{\text{domain}} I \rho dA}{A_c} + \frac{\int_{\text{domain}} I \rho w'^2 dA}{A_c} = \rho_c w_c^2 + [\rho w'^2]^c. \tag{A7}$$

Substituting this into Eq. (A6) gives

$$\frac{w_c}{A_c} \frac{\partial A_c \rho_c}{\partial t} + \rho_c \frac{\partial w_c}{\partial t} = -\frac{1}{A_c} \oint_c \mathbf{v}_H \cdot \hat{\mathbf{n}} \rho w dC - \frac{1}{A_c} \frac{\partial A_c \rho_c w_c^2}{\partial z} - \frac{1}{A_c} \frac{\partial A_c [\rho w'^2]^c}{\partial z} - \left[\frac{\partial p'}{\partial z}\right]^c + [\rho B]^c \frac{w_c}{A_c} \frac{\partial A_c \rho_c}{\partial t} + \rho_c \frac{\partial w_c}{\partial t}$$

$$= -\frac{1}{A_c} \oint_c \mathbf{v}_H \cdot \hat{\mathbf{n}} \rho w dC - \frac{w_c^2}{A_c} \frac{\partial A_c \rho_c}{\partial z} - \rho_c \frac{\partial w_c^2}{\partial z} - \frac{1}{A_c} \frac{\partial A_c [\rho w'^2]^c}{\partial z} - \left[\frac{\partial p'}{\partial z}\right]^c + [\rho B]^c. \tag{A8}$$

The continuity equation in (A3) can be substituted into the left-hand side:

$$\frac{w_c}{A_c} \left(-\oint_c \mathbf{v}_H \cdot \hat{\mathbf{n}} \rho dC - \frac{\partial A_c \rho_c w_c}{\partial z}\right) + \rho_c \frac{\partial w_c}{\partial t} = -\frac{1}{A_c} \oint_c \mathbf{v}_H \cdot \hat{\mathbf{n}} \rho w dC - \frac{w_c^2}{A_c} \frac{\partial A_c \rho_c}{\partial z} - \rho_c \frac{\partial w_c^2}{\partial z} - \frac{1}{A_c} \frac{\partial A_c [\rho w'^2]^c}{\partial z} - \left[\frac{\partial p'}{\partial z}\right]^c + [\rho B]^c,$$

$$\rho_c \frac{\partial w_c}{\partial t} = -\frac{1}{A_c} \oint_c \mathbf{v}_H \cdot \hat{\mathbf{n}} \rho (w - w_c) dC + \frac{w_c}{A_c} \frac{\partial \rho_c w_c A_c}{\partial z} - \frac{w_c^2}{A_c} \frac{\partial A_c \rho_c}{\partial z} - \rho_c \frac{\partial w_c^2}{\partial z} - \frac{1}{A_c} \frac{\partial A_c [\rho w'^2]^c}{\partial z} - \left[\frac{\partial p'}{\partial z}\right]^c + (\rho B)^c$$

$$= -\frac{1}{A_c} \oint_c \mathbf{v}_H \cdot \hat{\mathbf{n}} \rho (w - w_c) dC + \frac{w_c^2}{A_c} \frac{\partial \rho_c A_c}{\partial z} - \frac{w_c^2}{A_c} \frac{\partial A_c \rho_c}{\partial z} - \frac{\rho_c}{2} \frac{\partial w_c^2}{\partial z} - \frac{1}{A_c} \frac{\partial A_c [\rho w'^2]^c}{\partial z} - \left[\frac{\partial p'}{\partial z}\right]^c + (\rho B)^c,$$

$$\rho_c \frac{\partial w_c}{\partial t} = -\frac{1}{A_c}\oint \mathbf{v}_H \cdot \hat{\mathbf{n}}\rho(w - w_c)dC - \frac{\rho_c}{2}\frac{\partial w_c^2}{\partial z}$$

$$-\frac{1}{A_c}\frac{\partial A_c[\rho w'^2]^c}{\partial z} - \left[\frac{\partial p'}{\partial z}\right]^c + [\rho B]^c. \quad (A9)$$

Finally, we define a density-weighted buoyancy $B_c = \int_{\text{domain}} I\rho B dA / \int_{\text{domain}} I\rho dA = [\rho B]^c/\rho_c$. Dividing Eq. (A9) by ρ_c gives the following equation for the conditionally sampled vertical momentum budget:

$$\underbrace{\frac{\partial w_c}{\partial t}}_{\text{time tendency}} = \underbrace{B_c}_{\text{Term 1: buoyancy}} + \underbrace{-\frac{1}{\lfloor\rho\rfloor_c}\left|\frac{\partial p'}{\partial z}\right|_c}_{\text{Term 2: perturbation pressure gradient}}$$

$$+ \underbrace{-\frac{1}{A_c\lfloor\rho\rfloor_c}\oint_c \mathbf{v}_H \cdot \hat{\mathbf{n}}(w - w_c)\rho dC}_{\text{Term 3: momentum entrainment}}$$

$$+ \underbrace{-\frac{1}{2}\frac{\partial w_c^2}{\partial z}}_{\text{Term 4: vertical advection}} + \underbrace{-\frac{1}{A_c\lfloor\rho\rfloor_c}\frac{\partial A\lfloor\rho(w - w_c)\rfloor_c^2}{\partial z}}_{\text{Term 5: turbulent vertical flux}}.$$

$$(A10)$$

REFERENCES

Corr, C. A., and Coauthors, 2016: Observational evidence for the convective transport of dust over the central United States. *J. Geophys. Res. Atmos.*, **121**, 1306–1319, https://doi.org/10.1002/2015JD023789.

Cotton, W. R., and Coauthors, 2003: RAMS 2001: Current status and future directions. *Meteor. Atmos. Phys.*, **82**, 5–29, https://doi.org/10.1007/s00703-001-0584-9.

Davies-Jones, R., 2003: An expression for effective buoyancy in surroundings with horizontal density gradients. *J. Atmos. Sci.*, **60**, 2922–2925, https://doi.org/10.1175/1520-0469(2003)060<2922:AEFEBI>2.0.CO;2.

Dawe, J. T., and P. H. Austin, 2011: Interpolation of LES cloud surfaces for use in direct calculations of entrainment and detrainment. *Mon. Wea. Rev.*, **139**, 444–456, https://doi.org/10.1175/2010MWR3473.1.

DeMott, P. J., and Coauthors, 2010: Predicting global atmospheric ice nuclei distributions and their impacts on climate. *Proc. Natl. Acad. Sci. USA*, **107**, 11 217–11 222, https://doi.org/10.1073/pnas.0910818107.

de Roode, S. R., A. P. Siebesma, H. J. J. Jonker, and Y. de Voogd, 2012: Parameterization of the vertical velocity equation for shallow cumulus clouds. *Mon. Wea. Rev.*, **140**, 2424–2436, https://doi.org/10.1175/MWR-D-11-00277.1.

Drager, A. J., L. D. Grant, and S. C. van den Heever, 2020: Cold pool responses to changes in soil moisture. *J. Adv. Model. Earth Syst.*, **12**, e2019MS001922, https://doi.org/10.1029/2019MS001922.

Engström, A., A. M. L. Ekman, R. Krejci, J. Ström, M. de Reus, and C. Wang, 2008: Observational and modelling evidence of tropical deep convective clouds as a source of midtropospheric accumulation mode aerosols. *Geophys. Res. Lett.*, **35**, L23813, https://doi.org/10.1029/2008GL035817.

Fierro, A. O., J. Simpson, M. A. LeMone, J. M. Straka, and B. F. Smull, 2009: On how hot towers fuel the Hadley cell: An

observational and modeling study of line-organized convection in the equatorial trough from TOGA COARE. *J. Atmos. Sci.*, **66**, 2730–2746, https://doi.org/10.1175/2009JAS3017.1.

Harrington, J. Y., 1997: Effects of radiative and microphysical processes on simulated warm and transition season Arctic stratus. Ph.D. dissertation, Colorado State University, 289 pp.

Heikenfeld, M., P. J. Marinescu, M. Christensen, D. Watson-Parris, F. Senf, S. C. van den Heever, and P. Stier, 2019: tobac 1.2: Towards a flexible framework for tracking and analysis of clouds in diverse datasets. *Geosci. Model Dev.*, **12**, 4551–4570, https://doi.org/10.5194/gmd-12-4551-2019.

Jensen, M. P., and A. D. Del Genio, 2006: Factors limiting convective cloud-top height at the ARM Nauru Island climate research facility. *J. Climate*, **19**, 2105–2117, https://doi.org/10.1175/JCLI3722.1.

Johnson, R. H., T. M. Rickenbach, S. A. Rutledge, P. E. Ciesielski, and W. H. Schubert, 1999: Trimodal characteristics of tropical convection. *J. Climate*, **12**, 2397–2418, https://doi.org/10.1175/1520-0442(1999)012<2397:TCOTC>2.0.CO;2.

Kuang, Z., and C. S. Bretherton, 2006: A mass-flux scheme view of a high-resolution simulation of a transition from shallow to deep cumulus convection. *J. Atmos. Sci.*, **63**, 1895–1909, https://doi.org/10.1175/JAS3723.1.

Lau, K. M., and H. T. Wu, 2003: Warm rain processes over tropical oceans and climate implications. *Geophys. Res. Lett.*, **30**, 2290, https://doi.org/10.1029/2003GL018567.

Li, X., W.-K. Tao, H. Masunaga, G. Gu, and X. Zeng, 2013: Aerosol effects on cumulus congestus population over the tropical Pacific: A cloud-resolving modeling study. *J. Meteor. Soc. Japan*, **91**, 817–833, https://doi.org/10.2151/jmsj.2013-607.

Luo, Z., G. Y. Liu, G. L. Stephens, and R. H. Johnson, 2009: Terminal versus transient cumulus congestus: A CloudSat perspective. *Geophys. Res. Lett.*, **36**, L05808, https://doi.org/10.1029/2008GL036927.

Mapes, B., S. Tulich, J. Lin, and P. Zuidema, 2006: The mesoscale convection life cycle: Building block or prototype for large-scale tropical waves? *Dyn. Atmos. Oceans*, **42**, 3–29, https://doi.org/10.1016/j.dynatmoce.2006.03.003.

Marinescu, P. J., and Coauthors, 2021: Impacts of varying concentrations of cloud condensation nuclei on deep convective cloud updrafts—A multimodel assessment. *J. Atmos. Sci.*, **78**, 1147–1172, https://doi.org/10.1175/JAS-D-20-0200.1.

Masunaga, H., T. S. L'Ecuyer, and C. D. Kummerow, 2005: Variability in the characteristics of precipitation systems in the tropical Pacific. Part I: Spatial structure. *J. Climate*, **18**, 823–840, https://doi.org/10.1175/JCLI-3304.1.

McGee, C. J., and S. C. van den Heever, 2014: Latent heating and mixing due to entrainment in tropical deep convection. *J. Atmos. Sci.*, **71**, 816–832, https://doi.org/10.1175/JAS-D-13-0140.1.

Mecikalski, J. R., C. P. Jewett, J. M. Apke, and L. D. Carey, 2016: Analysis of cumulus cloud updrafts as observed with 1-min resolution super rapid scan GOES imagery. *Mon. Wea. Rev.*, **144**, 811–830, https://doi.org/10.1175/MWR-D-14-00399.1.

Meyers, M. P., R. L. Walko, J. Y. Harrington, and W. R. Cotton, 1997: New RAMS cloud microphysics parameterization. Part II: The two-moment scheme. *Atmos. Res.*, **45**, 3–39, https://doi.org/10.1016/S0169-8095(97)00018-5.

Morrison, H., and J. M. Peters, 2018: Theoretical expressions for the ascent rate of moist deep convective thermals. *J. Atmos. Sci.*, **75**, 1699–1719, https://doi.org/10.1175/JAS-D-17-0295.1.

Peters, J. M., 2016: The impact of effective buoyancy and dynamic pressure forcing on vertical velocities within two-dimensional

updrafts. *J. Atmos. Sci.*, **73**, 4531–4551, https://doi.org/10.1175/JAS-D-16-0016.1.

——, W. Hannah, and H. Morrison, 2019: The influence of vertical wind shear on moist thermals. *J. Atmos. Sci.*, **76**, 1645–1659, https://doi.org/10.1175/JAS-D-18-0296.1.

Posselt, D. J., S. C. van den Heever, and G. L. Stephens, 2008: Trimodal cloudiness and tropical stable layers in simulations of radiative convective equilibrium. *Geophys. Res. Lett.*, **35**, L08802, https://doi.org/10.1029/2007GL033029.

Redelsperger, J.-L., D. B. Parsons, and F. Guichard, 2002: Recovery processes and factors limiting cloud-top height following the arrival of a dry intrusion observed during TOGA COARE. *J. Atmos. Sci.*, **59**, 2438–2457, https://doi.org/10.1175/1520-0469(2002)059<2438:RPAFLC>2.0.CO;2.

Reid, J. S., and Coauthors, 2019: Observations and hypotheses related to low to middle free tropospheric aerosol, water vapor and altocumulus cloud layers within convective weather regimes: A SEAC⁴RS case study. *Atmos. Chem. Phys.*, **19**, 11 413–11 442, https://doi.org/10.5194/acp-19-11413-2019.

Riehl, H., and J. S. Malkus, 1958: On the heat balance in the equatorial trough zone. *Geophysica*, **6**, 503–558.

Romps, D. M., and A. B. Charn, 2015: Sticky thermals: Evidence for a dominant balance between buoyancy and drag in cloud updrafts. *J. Atmos. Sci.*, **72**, 2890–2901, https://doi.org/10.1175/JAS-D-15-0042.1.

Saleeby, S. M., and W. R. Cotton, 2004: A large-droplet mode and prognostic number concentration of cloud droplets in the Colorado State University Regional Atmospheric Modeling System (RAMS). Part I: Module descriptions and supercell test simulations. *J. Appl. Meteor. Climatol.*, **43**, 182–195, https://doi.org/10.1175/1520-0450(2004)043<0182:ALMAPN>2.0.CO;2.

——, and ——, 2008: A binned approach to cloud-droplet riming implemented in a bulk microphysics model. *J. Appl. Meteor. Climatol.*, **47**, 694–703, https://doi.org/10.1175/2007JAMC1664.1.

——, and S. C. van den Heever, 2013: Developments in the CSU-RAMS aerosol model: Emissions, nucleation, regeneration, deposition, and radiation. *J. Appl. Meteor. Climatol.*, **52**, 2601–2622, https://doi.org/10.1175/JAMC-D-12-0312.1.

Savre, J., 2021: Formation and maintenance of subsiding shells around non-precipitating and precipitating cumulus clouds. *Quart. J. Roy. Meteor. Soc.*, **147**, 728–745, https://doi.org/10.1002/qj.3942.

Sheffield, A. M., S. M. Saleeby, and S. C. van den Heever, 2015: Aerosol-induced mechanisms for cumulus congestus growth. *J. Geophys. Res. Atmos.*, **120**, 8941–8952, https://doi.org/10.1002/2015JD023743.

Sherwood, S. C., D. Hernández-Deckers, M. Colin, and F. Robinson, 2013: Slippery thermals and the cumulus entrainment paradox. *J. Atmos. Sci.*, **70**, 2426–2442, https://doi.org/10.1175/JAS-D-12-0220.1.

Siebesma, A. P., 1998: Shallow cumulus convection. *Buoyant Convection in Geophysical Flows*, E. J. Plate et al., Eds., NATO ASI Series, Springer, 441–486.

Takayabu, Y. N., S. Shige, W.-K. Tao, and N. Hirota, 2010: Shallow and deep latent heating modes over tropical oceans observed with TRMM PR spectral latent heating data. *J. Climate*, **23**, 2030–2046, https://doi.org/10.1175/2009JCLI3110.1.

Takemi, T., O. Hirayama, and C. Liu, 2004: Factors responsible for the vertical development of tropical oceanic cumulus convection. *Geophys. Res. Lett.*, **31**, L11109, https://doi.org/10.1029/2004GL020225.

Tian, Y., Z. Kuang, M. S. Singh, and J. Nie, 2019: The vertical momentum budget of shallow cumulus convection: Insights from a Lagrangian perspective. *J. Adv. Model. Earth Syst.*, **11**, 113–126, https://doi.org/10.1029/2018MS001451.

——, Y. Zhang, S. A. Klein, and C. Schumacher, 2021: Interpreting the diurnal cycle of clouds and precipitation in the ARM GoAmazon observations: Shallow to deep convection transition. *J. Geophys. Res. Atmos.*, **126**, e2020JD033766, https://doi.org/10.1029/2020JD033766.

van den Heever, S. C., G. L. Stephens, and N. B. Wood, 2011: Aerosol indirect effects on tropical convection characteristics under conditions of radiative–convective equilibrium. *J. Atmos. Sci.*, **68**, 699–718, https://doi.org/10.1175/2010JAS3603.1.

Verheggen, B., and Coauthors, 2007: Aerosol partitioning between the interstitial and the condensed phase in mixed-phase clouds. *J. Geophys. Res.*, **112**, D23202, https://doi.org/10.1029/2007JD008714.

Waite, M. L., and B. Khouider, 2010: The deepening of tropical convection by congestus preconditioning. *J. Atmos. Sci.*, **67**, 2601–2615, https://doi.org/10.1175/2010JAS3357.1.

Walko, R. L., and Coauthors, 2000: Coupled atmosphere–biophysics–hydrology models for environmental modeling. *J. Appl. Meteor. Climatol.*, **39**, 931–944, https://doi.org/10.1175/1520-0450(2000)039<0931:CABHMF>2.0.CO;2.

Wang, X., and M. Zhang, 2014: Vertical velocity in shallow convection for different plume types. *J. Adv. Model. Earth Syst.*, **6**, 478–489, https://doi.org/10.1002/2014MS000318.

Zipser, E. J., 2003: Some views on "hot towers" after 50 years of tropical field programs and two years of TRMM data. *Cloud Systems, Hurricanes, and the Tropical Rainfall Measuring Mission (TRMM): A Tribute to Dr. Joanne Simpson*, Meteor. Monogr., Amer. Meteor. Soc., 49–58.